An Improved Geometric Calibration Model for Spaceborne SAR Systems With a Case Study of Large-Scale Gaofen-3 Images

Yongjiu Feng, Zhenkun Lei, Xiaohua Tong, *Senior Member, IEEE*, Mengrong Xi, and Pengshuo Li

***Abstract*—Synthetic aperture radar (SAR) image positioning is commonly affected by factors such as platform instability, aging of onboard instruments, and changing observation environments. Thus, geometric calibration is needed to improve the accuracy of image positioning before mapping and application. An improved geometric calibration model for SAR images was developed, which does not require long-delayed meteorological data and geometric calibration fields. In this method, the standard atmospheric and Saastamoinen models (SAM-S) are combined for atmospheric delay correction, and this integrated method named SAM-S was used for the first time in SAR image geometric calibration. The method was applied to China's Gaofen-3 satellite and a case study was conducted in the Yangtze River Delta, where the weather is cloudy and rainy. By selecting three images, four images, and five images from eight candidate images with a bandwidth of 60 MHz for calibration experiments, where the geometric positioning accuracy was increasingly stable with more SAR images included in the combination. The root mean square of the calibrated SAR images was about 6 m for different combinations and the maximum error was about 12 m for all images. Two selected areas showed that the geometric calibration has reduced the geometric distortion, showing shapes in the SAR images close to the ground targets. The positioning accuracy improvement of Gaofen-3 images can help improve their application potential in global remote sensing mapping, land-use change monitoring, and ground target detection. The proposed geometric calibration method can also be applied to other SAR missions such as ERS, RADARSAT, and TerraSAR-X.**

***Index Terms*—Atmospheric delay correction, geometric calibration, grouped calibration, synthetic aperture radar, Yangtze river delt.**

I. Introduction

MICROWAVE remote sensing, especially synthetic aperture radar (SAR), is an effective technique for implementing earth observation [1], [2], [3]. Relying on the unique imaging advantages of microwave remote sensing, SAR images have been widely used to produce geographic information products, such as digital orthophoto maps (DOMs) and digital elevation models (DEMs), disaster prevention and mitigation, military object detection, and ship and oil spill detection [4], [5], [6], [7], [8]. Although SAR satellites have been calibrated on the ground before launch, various effects including the severe shocks of the satellite launch, the space environments with drastic temperature changes, and the aging of instruments may cause SAR sensors to operate deviating from the default settings [9], [10], [11]. Thus, geometric calibration is necessary to improve the positioning accuracy of SAR images to further release their application potential, especially in regions where optically multispectral and hyperspectral images cannot provide useful ground information.

Regular on-orbit geometric calibration can help eliminate the accumulated systematic errors in the whole life-cycle of satellites, and it is the most cost-effective way to improve the geometric positioning accuracy of SAR images [12], [13], [14]. The essence of SAR geometric calibration is to reduce the positioning difference for the same ground target between the field surveying and the geometric positioning model [15]. By estimating calibration parameters, the calibration models have been applied to improve the positioning accuracy of SAR images. The literature shows that the European Space Agency has achieved the calibrated geometric positioning accuracy of 20 m for ERS-1 and 10 m for ERS-2 [16], [17]. RADARSAT-2 and ALOS-PALSAR can also achieve a positioning accuracy of better than 10 m after geometric calibration [18], [19], [20]. With the reform of the design and manufacturing of onboard payloads and the improvement of geometric calibration tasks, the positioning accuracy of SAR images after geometric calibration may exceed the nominal spatial resolution of SAR images. The positioning accuracy of Sentinel-1A and Sentinel-1B images is about 7 m in the interferometric wide swath mode with a spatial resolution of 5 m$\times$20 m [21], [22]. The positioning accuracy of the TerraSAR-X images in the Stripmap model is about several centimeters after geometric calibration [23].

Earlier publications indicated that the positioning accuracy of TerraSAR-X in China is about several centimeters in the azimuth direction and 1 m in the slant range direction [24]. For China, Gaofen-3 is the first C-band fully-polarized SAR satellite with multiple imaging modes and global observation capability, and is freely available to international users [10], [25]. The positioning accuracy of TerraSAR-X images is better than 3 m in China after jointly geometric calibration with Gaofen-3 images using sparse

Manuscript received 16 March 2022; revised 9 May 2022, 15 June 2022, 9 July 2022, and 19 July 2022; accepted 31 July 2022. Date of publication 16 August 2022; date of current version 30 August 2022. This work was supported in part by the National Key R&D Program of China under Grant 2021YFB3900105-2 and in part by the National Natural Science Foundation of China under Grant 42071371. *(Corresponding author: Xiaohua Tong.)*

The authors are with the College of Surveying and Geo-Informatics, Shanghai 200092, China, and also with the Shanghai Key Laboratory of Space Mapping and Remote Sensing for Planetary Exploration, Tongji University, Shanghai 200092, China (e-mail: yjfeng@tongji.edu.cn; zhenkun_lei@tongji.edu.cn; xhtong@tongji.edu.cn; ximengrong@tongji.edu.cn; lipengshuo@tongji.edu.cn).

Digital Object Identifier 10.1109/JSTARS.2022.3198414

control points, where the root mean square (rms) of Gaofen-3 images is better than 7.5 m [26]. It is reported that the positioning accuracy of Gaofen-3 after joint geometric calibration in a large area is better than 8.5 m and the maximum error is less than 13 m [27]. Some indicated that the positioning accuracy of the calibrated Gaofen-3 images can reach 3 m when using calibration fields in northern China [9], [28]. The practice indicates a decaying geometric performance of SAR images in the areas far away from the geometric calibration fields, and the calibration experiments may yield different positioning accuracies at different times or places. Because of the decaying geometric performance of these images, an independent assessment should be reconducted in the areas far from the calibration fields [12]. The Gaofen-3 images are valuable earth observation datasets and their accuracy assessment and improvement are necessary for the consequent application. Because it is very costly to build geometric calibration fields, there is an urgent need to develop a suitable, convenient geometric calibration model to produce better Gaofen-3 SAR images.

To improve the positioning accuracy of SAR images, the geometric calibration models commonly need high-precision ground control points (GCPs). Useful GCPs can be derived using corner reflectors deployed in calibration fields, field surveying of natural feature points using global navigation satellite system (GNSS) devices, the panel coordinates and the elevation collected by DOMs, and the global DEMs [15], [22], [26], [29], [30], [31]. Although corner reflectors in calibration fields can provide high GCP accuracy, they are quite costly and their limited positions may not satisfy the geometric calibration in large-scale areas. In addition, field surveying is inefficient and unable to collect GCPs in areas (e.g., deserts and great mountains) that are inaccessible to humans. The rigorously verified high-precision DOMs and DEMs can provide useful GCPs, which can be applied to geometric calibration worldwide. Thus, the generic GCPs collection method is the key to constructing this improved geometric calibration model.

Considering the atmospheric delay of SAR microwave signals propagating in the earth's atmosphere, many earlier works adopted field-measured weather parameters or the weather reanalysis products to eliminate the delay, then improving the geometric calibration accuracy [32], [33], [34]. This requires collecting meteorological products before performing the geometric calibration. However, the weather reanalysis products are often released with a latency of several months, and only have a coarse spatiotemporal resolution [35], [36], [37], leading to the difficulty of collecting accurate, timely, and local atmospheric parameters. Because the products are usually derived from fusion and assimilation of multisource meteorological observation data, they may deviate from the actual atmospheric parameters [38], [39]. Although these long-delayed tropospheric correction methods and products have been widely used to perform atmospheric delay correction [34], [40], it is necessary to propose new methods to perform atmospheric delay correction for SAR geometric calibration. For this purpose, this article integrated the standard atmosphere model and the Saastamoinen model (SAM-S) in performing SAR geometric calibration. The standard atmosphere model provides the tropospheric parameters in near real-time and the Saastamoinen model derives the tropospheric delay [40], [41]. The SAM-S method has been widely applied to the tropospheric delay corrections in the GNSS pseudorange corrections and the multispectral image geometric corrections, which performs well worldwide [42], [43]. Earlier publications show that the modified positioning accuracy using the SAM-S method is about a decimeter-level lower than using the real meteorological data [40]. For large-scale geometric calibration, the decimeter-level loss in positioning accuracy is acceptable considering the efficiency and feasibility of the SAM-S method. Regarding the tradeoff between accuracy and efficiency, there is an urgent need to develop an improved geometric calibration model that can be applied to any region worldwide.

This article builds an improved geometric calibration model in SAR processing, with a case study in the Yangtze River Delta (YRD) area of China, where the most drastic land-use change was found in the last two decades. The YRD's cloudy, rainy weather has caused difficulties in mapping and updating using optically remote sensing [44], [45]. SAR has the advantage of capturing weather-independent ground images and thus provides an ideal data source for coastal mapping. [46], [47]. This article is aimed at developing an improved geometric calibration method of Gaofen-3 for large areas without the use of long-delayed meteorological data and geometric calibration fields. This improved model can help remote sensing users to perform geometric calibration at any time to improve the initial positioning performance of SAR images without complicated processing procedures. Also, it is suggested that this model can streamline the ON-orbit geometric calibration mission process of future SAR satellites and help to quickly start the operational services of SAR satellites. This article intends to answer the following questions: 1) Can the SAR geometric positioning accuracy be improved using the proposed geometric calibration model without long-delayed meteorological data and geometric calibration fields? and 2) Whether the proposed geometric calibration model can retrieve reliable calibration parameters and can stand the test of various calibration scenarios? To answer these questions, tropospheric delays were estimated in near real-time using the SAM-S method, and GCPs in DOMs and DEMs were collected as inputs to the geometric calibration model. To compare the positioning accuracy of Gaofen-3 images before and after geometric calibration, three scenarios of one-by-one calibration, joint calibration, and grouped calibration based on the SAR bandwidth were designed. To validate the applicability of the proposed geometric calibration method, Gaofen-3 images were collected in three regions of China for geometric calibration experiments in three imaging modes.

II. Methodology

A. Geometric Error Sources

The purpose of geometric calibration is to eliminate the systematic errors of SAR satellites, then establish the accurate mapping relationship between SAR images and the earth's surface [15], [28]. Specifically, the electronic time-delays of digital signal processors (DSP) and the atmospheric delays caused the slant range measurement errors, while the time-shifts between onboard DSP and GNSS devices caused the along-track range measurement errors [22], [27], [33]. Fig. 1 shows that there are

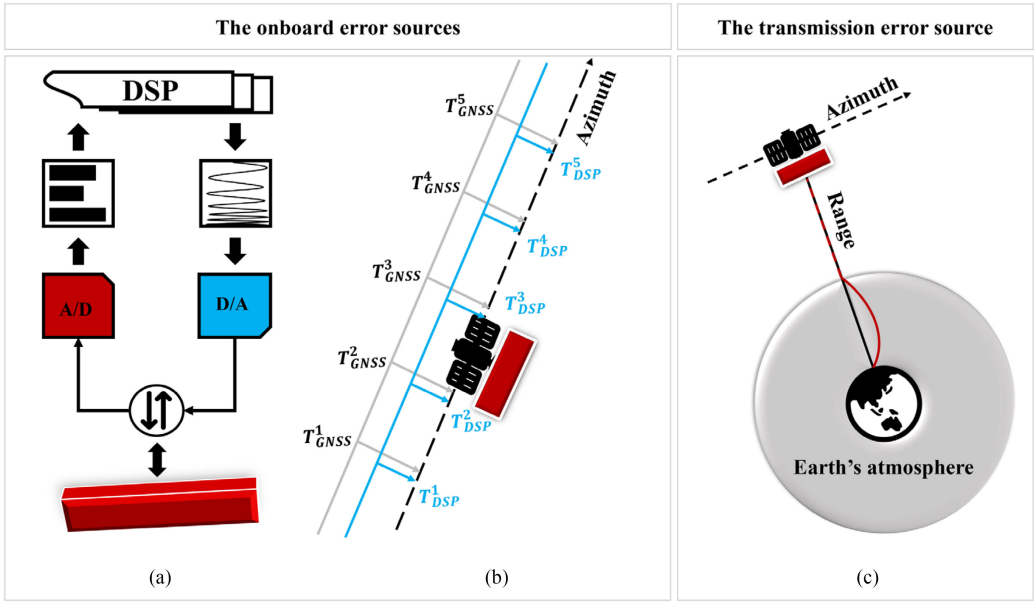

Fig. 1. Three main sources that cause the geometric positioning errors of SAR images. (a) The electronic time-delays. (b) The DSP-GNSS time-shifts. (c) The atmospheric delays.

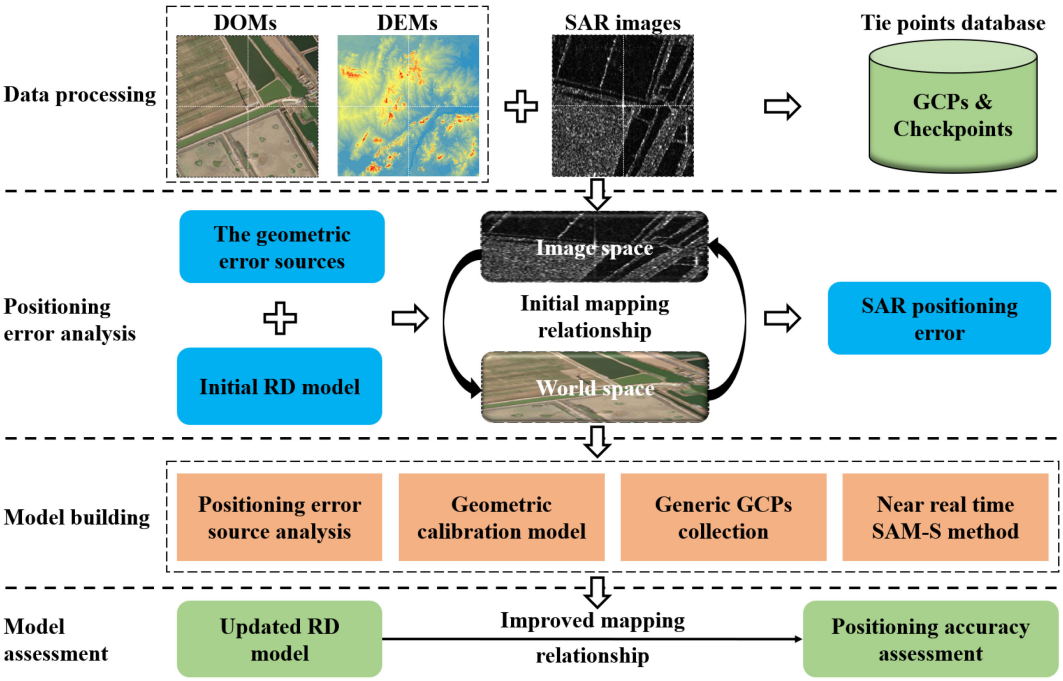

Fig. 2. Workflow of the improved SAR geometric calibration method.

two onboard-error sources and one transmission-error source. The electronic time-delays, which are caused by the transmit and receive processing of signals within the DSP, usually lead to measurement errors of the initial slant range in the range direction [see Fig. 1(a)]. The DSP-GNSS time-shifts, which are caused by the time reference difference between the DSP and GNSS devices, usually lead to the inconsistency of imaging timestamps in the azimuth direction [see Fig. 1(b)]. The atmospheric delay caused by the reflection of microwave signals in the earth's atmosphere usually results in an inaccurate measurement of the slant range that is greater than the actual distance between the phase center of the SAR satellite antenna and the observation target [see Fig. 1(c)].

B. *Improved Geometric Calibration Workflow*

Fig. 2 shows the crucial processes of the improved geometric calibration method, which includes six steps.

1) Collecting the coordinates of SAR images and the earth-centered-earth-fixed (ECEF) coordinates of the tie points

in the SAR images, DOMs, and DEMs, where the plane coordinates are provided by DOMs and the elevation is provided by DEMs.
2) Based on the auxiliary files of the SAR images, the initial Range Doppler (RD) model was built to establish the relationship between the SAR image space and the world space.
3) The initial RD model was used to quantify the positioning errors of SAR images after geometric positioning, with selected GCPs as references.
4) A GCP acquisition scenario was then developed and the SAM-S method was used to construct an improved geometric calibration model for estimating the calibration parameters of the SAR satellite.
5) The calibration parameters were applied to update the RD model.
6) Finally, the feasibility of this method was verified by a case study of Gaofen3 images in YRD.

C. Geometric Calibration Model

The onboard systematic errors that lead to decreases in SAR image positioning accuracy are consistent and reoccurring over time. The quality of geometric calibration depends on the inherent stability of the SAR imaging system and its capability to determine the geometric features [9], [15]. To eliminate the systematic errors and improve the absolute positioning accuracy of SAR images, precise GCPs are usually adopted to estimate the parameters of the geometric calibration models, which can be given by [28]

$$\begin{cases} t_{rng} = t_{rng0} + \Delta t_{rng} + \frac{x}{f_r} + \frac{R_{\text{delay}}}{C} \\ t_{azi} = t_{azi0} + \Delta t_{azi} + \frac{y}{f_a} \end{cases} \tag{1}$$

where t_{rng} and t_{azi} are the record timestamps of the target (x, y) in the range and azimuth directions of the SAR imaging system, respectively, t_{rng0} and t_{azi0} are the initial time in the range and azimuth directions, respectively, R_{delay} is the troposphere delay caused by the signal propagation in the atmosphere, which can be estimated using the SAM-S method, Δt_{rng} is the electronic time-delay of the SAR imaging system, Δt_{azi} is the DSP-GNSS time-shift, f_r is the radar pulse sampling frequency, f_a is the pulse repetition frequency, and C is the speed of light in vacuum.

SAR satellites are featured by side-looking imaging, and they can adjust the bandwidth of the emission microwave signal according to different incident angles to achieve similar/identical spatial resolution in the same imaging mode [28], [34], [48]. Even in the same imaging mode, different bandwidths can lead to different electronic time-delays. Usually, the SAR imaging in a large-scale area is related to different bandwidths and pulse widths, which are needed to be considered when conducting geometric calibration.

D. Atmospheric Delay Correction

To perform a robust estimation of the main parameters of SAR geometric calibration, the atmospheric delay should be eliminated first [33]. This article adopts the standard atmosphere model (SAM) to estimate the atmospheric parameters in near real-time, then used the Saastamoinen model (S model) to calculate the tropospheric delay. The combined model was called SAM-S, where the SAM can be given by [49], [50]

$$\begin{cases} \text{Press} = 1013.25 \times \left(1 - 2.2557 \times 10^{-5} h\right)^{5.2568} \\ \text{Temp} = 15.0 - 6.5 \times 10^{-3} h + 273.15 \\ W_{\text{press}} = 6.108 \times e^{\frac{17.15\text{Temp} - 4684.0}{\text{Temp} - 38.45}} \times w \end{cases} \tag{2}$$

where Press indicates the atmospheric pressure, Temp indicates the thermodynamic temperature, h indicates the elevation of the ground target, w indicates the relative humidity, which is assigned to 0.7 in the absence of observed atmospheric parameters, and W_{press} indicates the partial pressure of water vapor.

In the Saastamoinen model of calculating the tropospheric delay, the zenith tropospheric delay (ZTD) can be represented by the sum of zenith hydrostatic delay (ZHD) and zenith wet delay (ZWD), where ZHD typically accounts for more than 90% of ZTD. The tropospheric delay can be given by [40]

$$\begin{cases} \text{ZHD} = \frac{0.0022768 \times \text{Press}}{1 + 0.00266 \times \cos(2\varphi) - 0.00028 \times h} \\ \text{ZWD} = 0.0022768 \times \left(\frac{1255}{\text{Temp}} + 0.05\right) \times W_{\text{press}} \\ \text{tropospheric delay} = \frac{\text{ZTD}}{\cos(\varphi)} = \frac{\text{ZHD} + \text{ZWD}}{\cos(\varphi)} \end{cases} \tag{3}$$

where φ is the satellite incident angle and Press, Temp, and W_{press} is presented in the previous equation.

The neutral molecules in the atmosphere higher than the tropospheric layer (above the earth's surface at 50 km) are ionized due to the excitation of high-energy rays, reducing the speed of electromagnetic waves and then causing the slant range measurement errors of the radar imaging system. The ionospheric delay can be defined as [32], [51]

$$\text{ionospheric delay} = \frac{40.28 \times \text{TEC}}{f^2 \cos(\varphi)} \tag{4}$$

where TEC is the total electron content and f is the radar center frequency. The TEC data can be automatically collected using a web crawler at the Center for Orbit Determination in Europe (ftp.aiub.unibe.ch/CODE/IONO), which provides global TEC maps every two hours.

E. Solution of the Geometric Calibration Model

To construct the geometric calibration model, this article first explores the relationship between SAR image pixels and ground targets. The RD model describes the geometric relationship between the satellite and the ground targets, and is a rigorous geometric imaging model for spaceborne SAR sensors [52]. The model has most widely been used in SAR imaging geolocation processing to derive high positioning accuracy because it is independent of the sensor attitude [53], [54]. The RD model includes all imaging geometric parameters and is ideal for geometric calibration. The elements of the RD model can be

written as [27]

$$\begin{cases} X_s = a_0 + a_1 t_{azi} + a_2 t_{azi}^2 + a_3 t_{azi}^3 \\ Y_s = b_0 + b_1 t_{azi} + b_2 t_{azi}^2 + b_3 t_{azi}^3 \\ Z_s = c_0 + c_1 t_{azi} + c_2 t_{azi}^2 + c_3 t_{azi}^3 \\ V_x = a_1 + 2a_2 t_{azi} + 3a_3 t_{azi}^2 \\ V_y = b_1 + 2b_2 t_{azi} + 3b_3 t_{azi}^2 \\ V_z = c_1 + 2c_2 t_{azi} + 3c_3 t_{azi}^2 \\ t_{azi} = t_{azi0} + \frac{y}{f_a} \\ R = \sqrt{(X_s - X)^2 + (Y_s - Y)^2 + (Z_s - Z)^2} \end{cases} \tag{5}$$

where (a_0, a_1, a_2, a_3, b_0, b_1, b_2, b_3, c_0, c_1, c_2, c_3) are the coefficients of the polynomial that describes the satellite orbit, (*X, Y, Z*) and (*Xs, Ys, Zs*) are the coordinates of the ground target and the satellite in the ECEF coordinate system, respectively, and *R* is the slant range between the satellite and the ground target.

The RD model can be given by [26], [55]

$$\begin{cases} R - \left(t_{rng0} + \frac{x}{f_r}\right) \cdot \frac{C}{2} = 0 \\ \frac{-2}{\lambda R}\left[(X_s - X) V_x + (Y_s - Y) V_y + (Z_s - Z) V_z\right] = 0 \\ \frac{(X^2 + Y^2)}{(a+h)^2} + \frac{Z^2}{(b+h)^2} - 1 = 0 \end{cases} \tag{6}$$

where (*a*, *b*) are the semimajor axis and semiminor axis of the earth and *h* is the elevation of the ground target.

The geometric model can be solved with the input of GCPs based on the principle of least squares. The correction of iterative solution for the imaging geometric parameters can be calculated with only one or more GCPs, where more GCPs could improve the reliability of the geometric calibration [26]. However, collecting high-precision GCPs could increase the cost, especially in harsh environments that are inaccessible to humans. For geometric calibration and image positioning accuracy verification in large-scale areas, the demand for excessive GCPs in different regions makes it difficult to collect sufficient, suitable GCPs from geometric calibration fields or field surveying. Collecting GCPs from DOMs and DEMs may be the most economical way to perform the SAR geometric calibration. The GCP selection is to find ground target points with strong reflections, which are commonly surrounded by weak back-scattering objects. Because it is difficult to visually identify ground targets from SAR images, it requires finding features of significant geometric and reflective characteristics. DOMs from Google Earth and Bing Map can provide the plane coordinates of GCPs while freely available DEMs (e.g., SRTM DEM, ALOS DEM, and NASA DEM) can provide the elevation of GCPs. The gray weighted centroid (GWC) method was applied to search for the strongest scattering point.

A single image-based geometric calibration scenario (one-by-one) can best improve the positioning accuracy of the SAR image, and can also be used for the calibration of SAR images nearby. A joint geometric calibration scenario is to construct the model using multiple SAR images, which can apply to all the images over time. The joint scenario can realize a more robust estimation of SAR imaging system errors, thus improving the positioning accuracy and reducing the negative impacts of inaccurate GCPs on the definition of model parameters.

F. Three Calibration Scenarios

To examine the reliability of the proposed SAR geometric calibration model, three calibration scenarios were performed in this study, including one-by-one calibration, joint calibration, and grouped calibration.

1) The one-by-one calibration method is carried out for one image only, where the initial calibration parameters are calculated according to the GCPs in the same image and the geometric calibration model. The final calibration parameters can be calculated based on the least-squares method.
2) The joint geometric calibration method is carried out for multiple images, where some (or all) of these containing GCPs are selected for calibration and the rest are used for validation. The initial calibration parameters of each image in calibration are calculated based on the GCPs and the geometric calibration model, then the least-squares method is used to derive the optimal calibration parameters for multiple images in calibration.
3) The grouped calibration method is also carried out for multiple images (e.g., *n*), where some of these (e.g., *s* images from total *n* images) are randomly selected for the calibration, generating C_n^s combinations of calibration schemes. For each combination, the joint geometric calibration method is used to derive calibration parameters.

III. Application and the Results

A. Study Area and Datasets

This study area covers more than 170 000 km^2 in YRD, including part of Anhui province, Jiangsu province, and Zhejiang province, and all areas of Shanghai city (see Fig. 3). Cloudy and rainy weather in YRD leads to the failure of optical remote sensing satellites in capturing the earth's surface, while microwave remote sensing (especially SAR satellites) can provide high-resolution, day-and-night, and weather-independent images. SAR satellites provide efficient data sources for coastal area mapping tasks [46], [56]. The geometric performance improvement of Gaofen-3 SAR images using the geometric calibration model would effectively release the potential of producing fundamental geographic information products. Therefore, this study area is an ideal choice for the positioning accuracy assessment of the geometric calibration model. In addition, 6 images of FSII mode in Beijing and 4 images of FSII mode in Xinjiang were acquired to verify the applicability of the model. All images were acquired with different combinations of bandwidth and pulse width between December 2016 and September 2020 (see Table I).

For the Gaofen-3 satellite, the FSII mode SAR images are a suitable choice for large-scale mapping tasks because they satisfy the spatial resolution (10 m) and image swath (100 km). In Fig. 3, both the control points and checkpoints are GCPs selected in advance, where the former was used to solve the calibration parameters while the latter was used to validate the geometric calibration model and the positioning accuracy. In addition, the reliability of geometric calibration is highly related to the accuracy of GCPs. In this article, each SAR image includes

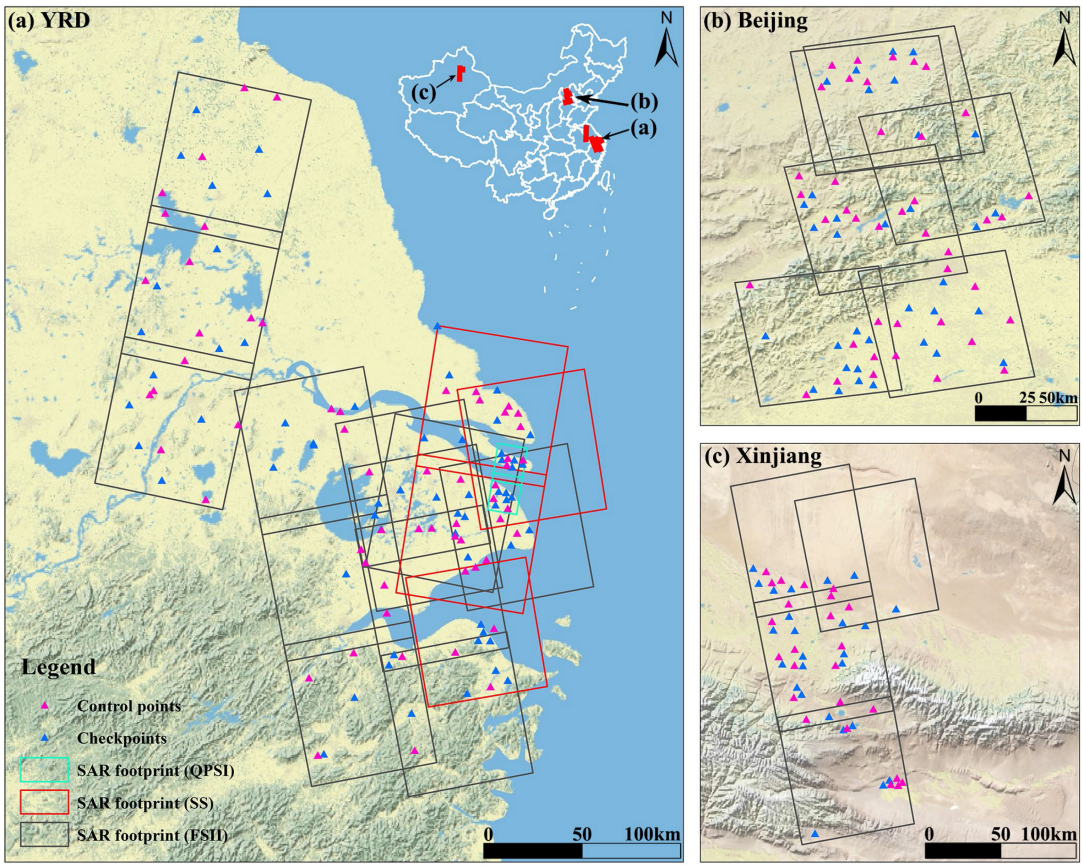

Fig. 3. SAR image footprints that cover parts of YRD, Beijing, and Xinjiang. The images of YRD were used to verify the effectiveness of the model (Experiment-1), and the images from Beijing and Xinjiang were used to verify the model's applicability.

at least three control points and five checkpoints (see Fig. 3), which could not be easily prepared using a calibration field because of the high construction cost.

Fig. 4 shows four pairs of targets selected both in the aerial orthophotos with meter-level positioning accuracy and in the uncalibrated Gaofen-3 SAR images. All the GCPs were collected by the aerial orthophotos provided by the Shanghai Surveying and Mapping Institute. The GCPs in the Bing Maps (multispectral images) were matched and linked to the Gaofen-3 SAR images (see Fig. 4). The tie points were identified and then recorded their coordinates in both the geodetic coordinate system and the SAR image coordinate system. The geodetic coordinates were converted to the ECEF coordinates based on the WGS84 reference ellipsoid. The elevation values of the tie points were provided by SRTM DEM. Due to the severe speckle noise in SAR images, the targets usually cannot be identified clearly. To ensure accuracy, the intersection points of roads and the relatively fixed features near rivers and lakes were selected as the candidate GCPs. For example, a wind turbine is a suitable target that indicates similar characteristics to a corner reflector in SAR images.

B. Atmospheric Delay Estimation

It has been acknowledged that the product of the International GNSS Service (IGS) is the benchmark [57], [58]. However, the IGS product only detects specific monitoring stations that may not be in the region of interest. In this regard, if the results of the SAM-S method approximate those of IGS in the atmospheric delay correction, the method can be properly applied elsewhere. The IGS product was compared with the SAM-S approach using data from three IGS stations (i.e., BJFS in Beijing, SHAO in Shanghai, and URAM in Xinjiang). Table II shows the differences in the atmospheric delays between the IGS and the SAM-S method, at the three IGS stations at the time of SAR imaging. The incident angle of the Gaofen-3 SAR sensor generally ranges from 20° to 40°, and the related difference in the atmospheric delays ranges from 0.06 m to 0.4 m with a mean value of 0.2 m. By projecting the atmospheric delay into the ground, the caused ground error is less than 1.2 m with a mean value of about 0.5 m. This error is far smaller than the SAR image's spatial resolution (10 m). This proves the effectiveness of the SAM-S model, which can be used to perform fast atmospheric delay correction for regular geometric calibration tasks in large-scale areas.

C. Preliminary Geometric Calibration

To verify the model accuracy and the Gaofen-3 image's geometric performance in YRD, multiple experiments were performed to inspect the geometric positioning accuracy before and after geometric calibration. Table III shows that, before calibration, the rms of the collected Gaofen-3 images is 38.41 m. After one-by-one calibration and using each image as both the calibration and validation, the rms of the calibrated images is

TABLE I
GAOFEN-3 SAR IMAGES SELECTED FOR VERIFYING THE GEOMETRIC CALIBRATION MODEL

Study area	Image No.	Imaging time	Orbit direction	Imaging mode	Incident angle (°)	Bandwidth (MHz)	Pulse width (μs)
YRD	L9244	2016/12/29 21:44	Descending	QPSI	47.44	30	24.99
	L9245	2016/12/29 21:44	Descending	QPSI	47.44	30	24.99
	L9776	2018/05/27 10:04	Ascending	SS	48.91	20	45
	L5285	2018-05-21 10:05	Ascending	SS	45.59	20	45
	L2205	2018-05-29 21:47	Descending	SS	49.08	20	45
	L2206	2018-05-29 21:47	Descending	SS	49.09	20	45
	L4147	2018/07/05 22:03	Descending	FSII	28.34	80	45
	L8411	2018/07/24 22:16	Descending	FSII	23.01	100	45
	L8412	2018/07/24 22:16	Descending	FSII	23.05	100	45
	L8413	2018/07/24 22:16	Descending	FSII	23.08	100	45
	L4533	2018/10/24 09:57	Ascending	FSII	35.09	60	45
	L4534	2018/10/24 09:57	Ascending	FSII	35.01	60	45
	L9743	2018/11/10 09:54	Ascending	FSII	35.08	60	45
	L6893	2018/11/22 09:58	Ascending	FSII	34.99	60	45
	L0241	2019/01/02 10:01	Ascending	FSII	34.96	60	45
	L0242	2019/01/02 10:01	Ascending	FSII	34.94	60	45
	L0243	2019/01/02 10:01	Ascending	FSII	34.92	60	45
	L1348	2019/05/15 09:58	Ascending	FSII	35.20	60	45
Beijing	L2078	2018-07-26 10:24	Ascending	FSII	49.00	50	45
	L7076	2018-11-29 10:10	Ascending	FSII	34.92	50	45
	L7078	2018-11-29 10:11	Ascending	FSII	35.05	50	45
	L2263	2019/06/22 10:28	Ascending	FSII	48.92	50	45
	L0186	2020/09/14 10:09	Ascending	FSII	28.19	50	45
	L5402	2020/07/23 10:02	Ascending	FSII	22.88	50	45
Xinjiang	L4384	2018-09-10 12:01	Ascending	FSII	35.14	50	45
	L4385	2018-09-10 12:02	Ascending	FSII	35.07	50	45
	L4386	2018/09/10 12:02	Ascending	FSII	35.03	50	45
	L6280	2018/12/23 11:59	Ascending	FSII	34.43	50	45

TABLE II
COMPARISON OF THE ESTIMATIONS OF THE ZTD BETWEEN IGS AND SAM-S

Method/Source	Observation station	ZTD (m)			Summary statistics (m)			
		2018/07/24 22:16:08	2018/10/24 09:57:40	2019/01/02 10:01:14	Min	Mean	Max	Std Dev
Benchmark: IGS	BJFS	2.6149	2.3699	2.3383	2.1142	2.3729	2.7038	0.1926
	SHAO	2.7038	2.4629	2.4233				
	URUM	2.1719	2.1142	2.1570				
The used method: SAM-S	BJFS	2.3081	2.3081	2.3081	2.3072	2.3084	2.3098	0.0011
	SHAO	2.3098	2.3098	2.3098				
	URUM	2.3072	2.3072	2.3072				
Difference (SAM-S minus IGS)	BJFS	0.3068	0.0618	0.0302	0.0302	0.1709	0.3939	0.1084
	SHAO	0.3939	0.1531	0.1135				
	URUM	-0.1353	-0.1930	-0.1502				

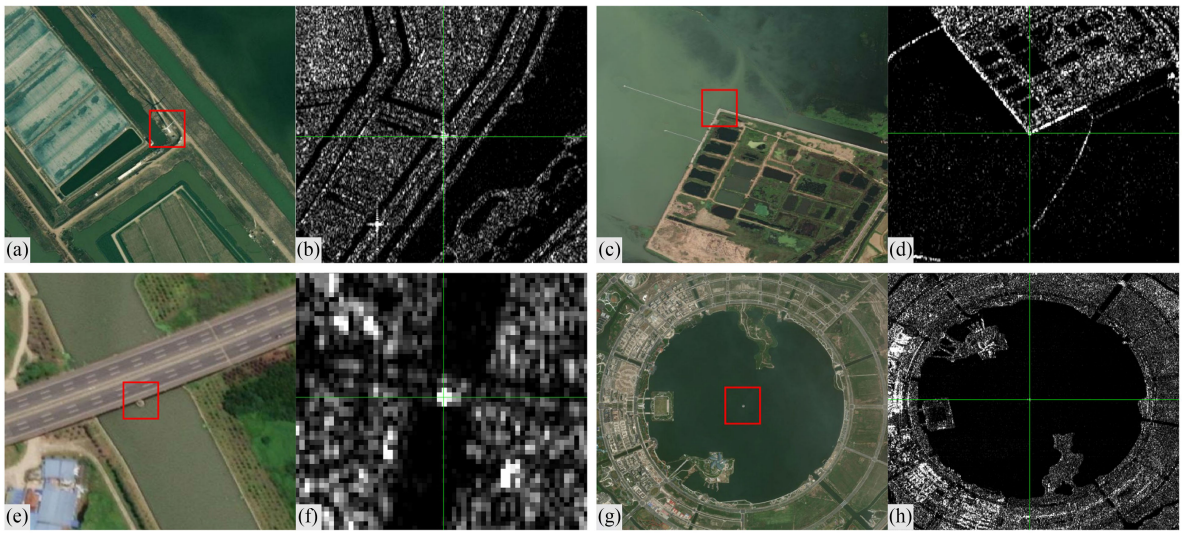

Fig. 4. Typical targets selected in both the Bing Maps (multispectral images) and the Gaofen-3 SAR images. For the same area, both the red rectangle center and the green-cross link to the same ground target. In this figure, (a), (b) a wind turbine, (c), (d) the corner of a dam, (e), (f) a bridge pier, and (g), (h) a metal sculpture in an artificial lake.

TABLE III
COMPARISON OF THE ONE-BY-ONE CALIBRATION AND JOINT CALIBRATION SCENARIOS

Image	The one-by-one calibration scenario				The joint calibration scenario			
	Slant range correction (m)	Imaging time correction (s)	Positioning accuracy (m)		Slant range correction (m)	Imaging time correction (s)	Positioning accuracy (m)	
			Before	After			Before	After
L4147 (80MHz)	-17.27	-0.0062	34.83	7.04	-17.15	-0.0048	34.83	17.86
L8411 (100MHz)	-18.10	-0.0067	50.32	6.34			50.32	14.04
L8412 (100MHz)	-19.42	-0.0062	55.43	6.63			55.43	16.69
L8413 (100MHz)	-20.20	-0.0064	64.14	4.11			64.14	19.64
L4533 (60MHz)	-13.91	-0.0042	24.25	3.50			24.25	7.97
L4534 (60MHz)	-15.20	-0.0052	26.27	4.75			26.27	7.79
L9743 (60MHz)	-14.33	-0.0048	26.01	4.85			26.01	4.96
L6893 (60MHz)	-13.82	-0.0057	36.94	7.12			36.94	6.71
L0241 (60MHz)	-15.72	-0.0045	24.92	3.02			24.92	5.63
L0242 (60MHz)	-18.71	-0.0060	29.93	3.98			29.93	5.15
L0243 (60MHz)	-18.76	-0.0068	35.32	1.10			35.32	7.72
L1348 (60MHz)	-15.06	-0.0055	26.12	8.57			26.12	8.32
RMS (all)	/	/	38.41	5.47	/		38.41	11.41
RMS (60MHz)	/	/	29.10	5.10	/		29.10	6.90

improved to 5.47 m, with a maximum error is 8.57 m. The one-by-one calibration shows that the range of initial slant range correction is 6.38 m (–20.20 m versus –13.82 m), and the range of imaging time correction is 2.6 ms (–6.8 ms versus –4.2 ms); these corrections vary greatly, thus, the correction of an image cannot be applied to another. The joint calibration method applied to all images, used as both calibration and validation, shows a slant range correction of –17.15 m and an imaging time correction of –0.0048 s, resulting in an rms value of 11.41 m for positioning accuracy. Compared to the one-by-one calibration, the accuracy decrease in joint calibration is largely caused by the first four images with a bandwidth 80 MHz or 100 MHz. By excluding these four images, the positioning accuracy of the remaining images with a bandwidth 60 MHz is 6.90 m after joint calibration (see Table III). This indicates that the bandwidth also greatly affects the geometric calibration of SAR images, and more accurate calibration should be grouped the SAR images based on their bandwidths.

D. Grouped Geometric Calibration

To investigate the optimal group of images, further experiments were done to select three, four, and five images from eight candidate images with a bandwidth of 60 MHz as calibration and all images as validation. There are 56 combinations of three images, 70 combinations of four images, and 56 combinations

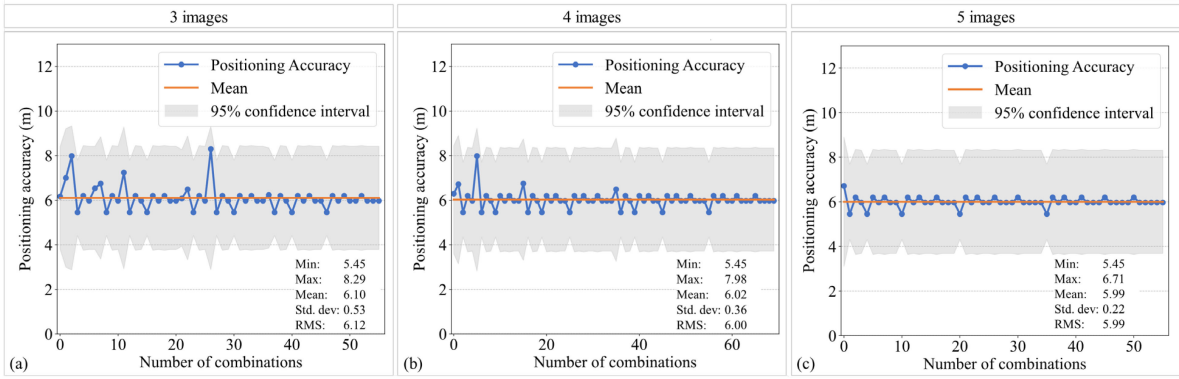

Fig. 5. Changes in geometric positioning accuracy when using different combinations of images.

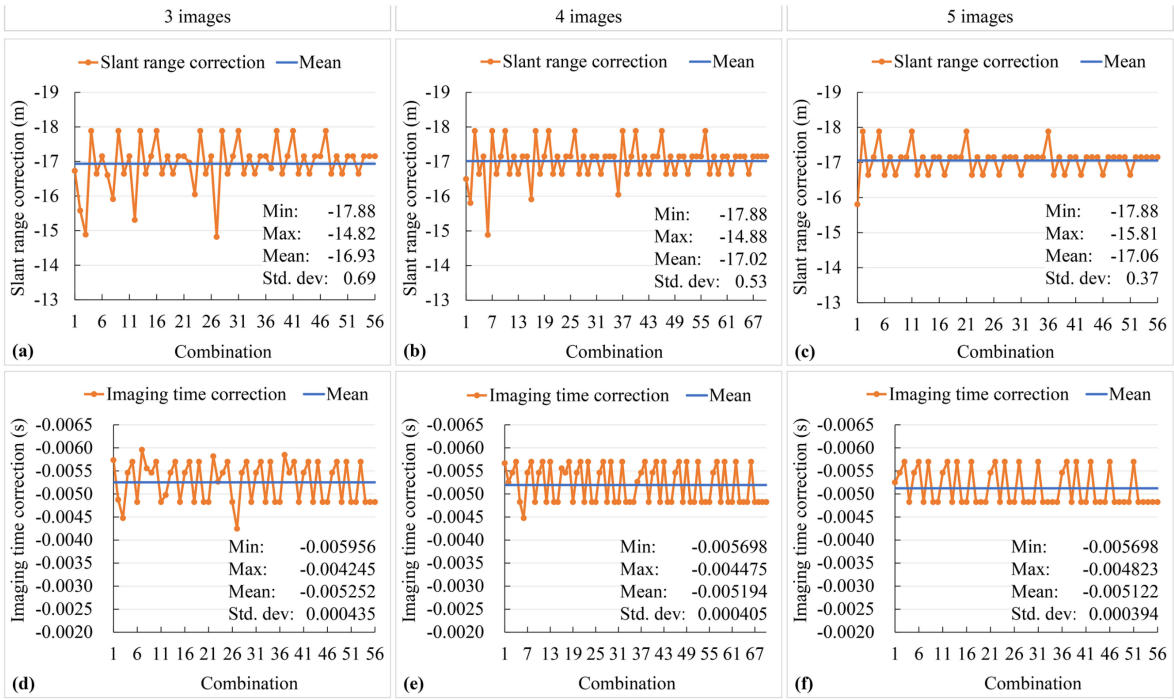

Fig. 6. Changes in the calibration parameters when using different combinations of 3 images (a) and (d), 4 images (b) and (e), and 5 images (c) and (f).

of five images (see Fig. 5). The geometric positioning accuracy of the grouped calibration is increasingly stable when more SAR images are included in the combination. However, it is similar to the previous joint calibration (see Table III) and could increase the workload when using more than 5 SAR images. Fig. 5 shows that the rms of the calibrated SAR images is about 6 m (the yellow line) with a 95% confidence interval for three types of combinations (three, four, or five images) and the maximum error is less than 11 m. As more images are included in the combination, the positioning accuracy is improved as shown by the decreased maximum and mean errors, and the calibration results are more reliable, as shown by the decreased standard deviation.

To examine the sensitivity of the calibration parameters, this article checked their changes related to different combinations of images. Using the grouped calibration method, the slant range and imaging time corrections are closer to their mean lines when using more images (see Fig. 6). For example, the slant range correction is about –17.06 m and the imaging time correction is about –0.0051 s for the combination of five images. Similar to the positioning accuracy, the range (Max minus Min) and the standard deviation of these two corrections decrease when more images are included in the calculation. The improved calibration parameters enhance the geometric calibration accuracy, thus avoiding using costly geometric calibration fields and the accurate atmospheric parameters that are difficult to acquire.

E. Applicability Assessment

To assess the applicability of the improved model, geometric calibration of the SAR images was performed in Beijing and Xinjiang. In the Experiment-2 scenario, a joint geometric calibration was performed in Beijing and obtained an rms of 6.75 m. The calibration parameters were then applied to the Xinjiang

TABLE IV
CROSS-VALIDATION OF GEOMETRIC CALIBRATION RESULTS IN BEIJING AND XINJIANG

Scenario	Location	Used to	Image	Slant range correction (m)	Imaging time correction (s)	Positioning accuracy (m)	
						Before	After
Experiment-2	Beijing	Calibrate	L2078	-17.96	-0.0078	17.97	6.11
			L7078			26.93	5.55
			L7076			28.04	6.40
			L2263			18.10	6.04
			L5402			43.80	10.10
			L0186			34.77	5.11
	Xinjiang	Validate	L4386	-17.96 (Same as above)	-0.0078 (Same as above)	22.83	10.79
			L4385			26.95	6.99
			L4384			25.83	5.50
			L6280			24.20	9.21
	RMS (Beijing)					29.69	6.75
	RMS (Xinjiang)					25.00	8.37
Experiment-3	Xinjiang	Calibrate	L4386	-18.98	-0.0050	22.83	12.07
			L4385			26.95	7.30
			L4384			25.83	7.39
			L6280			24.20	10.30
	Beijing	Validate	L2078	-18.98 (Same as above)	-0.0050 (Same as above)	17.97	7.57
			L7078			26.93	7.17
			L7076			28.04	7.44
			L2263			18.10	7.47
			L5402			43.80	12.51
			L0186			34.77	7.44
	RMS (Xinjiang)					25.00	9.48
	RMS (Beijing)					29.69	8.48

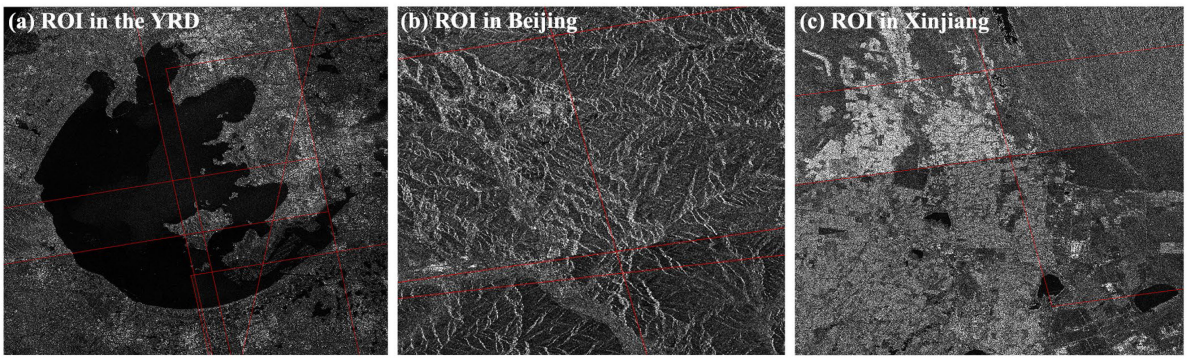

Fig. 7. Overlapping areas of adjacent images in YRD (a), Beijing (b), and Xinjiang (c) show good positioning accuracy and geometric consistency after geometric calibration.

images to verify the applicability of the model, and the rms for Xinjiang was 8.37 m (see Table IV). In the Experiment-three scenario, a joint geometric calibration was performed in Xinjiang that yielded an rms of 9.48 m, then applied the calibration parameters to images of Beijing to verify the model applicability, and the rms of Beijing was 8.48 m. Compared to the results of Experiment-3, the positioning accuracy of images in Beijing calibrated using the parameters of Experiment-2 is better (see Table IV).

Specifically, linear targets (e.g., boundaries of rivers and straight roads) were selected to check the positioning accuracy of the SAR images, especially the geometric consistency between SAR images before and after calibration. Fig. 7 shows that the three regions mosaicked using SAR images from YRD, Beijing and Xinjiang have no seamlines after geometric calibration, indicating the model has good geometric consistency. Fig. 8(a) shows the locations of the two selected check regions in YRD. Fig. 8(b) shows that, before calibration, the path in the farmland yields irregular geometric offset; while it is corrected to the red line after the calibration and the shape many accords to the real path (the red lines in Fig. 8(c)–(d) are parallel lines). Fig. 8(e) shows that the image of the river is distorted before calibration,

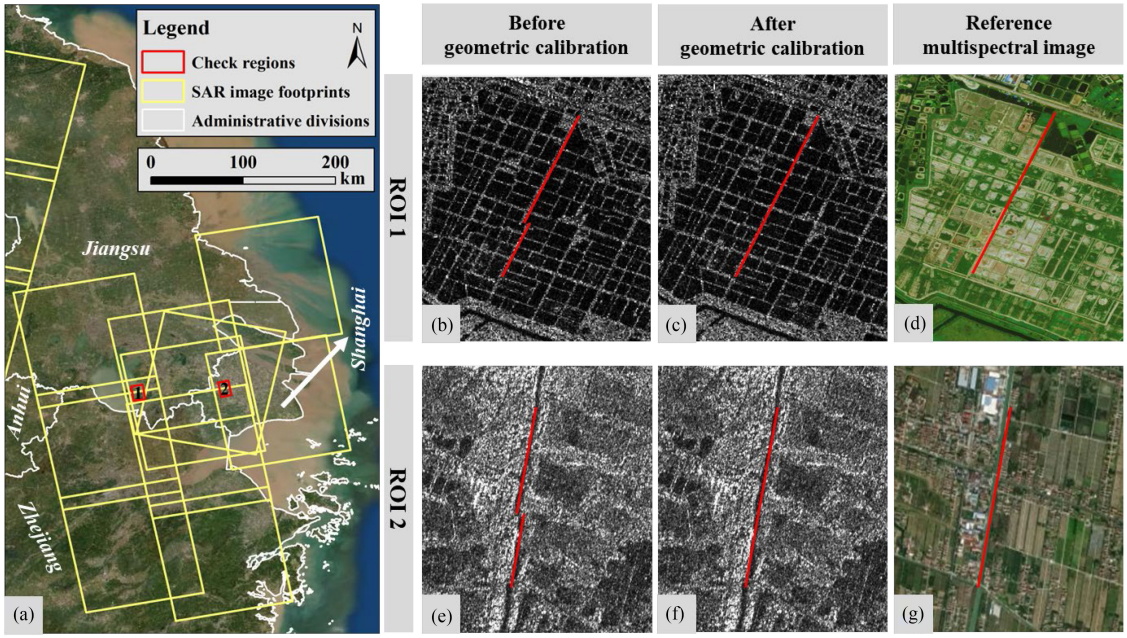

Fig. 8. Geometric consistency of linear targets in YRD is improved after the geometric calibration.

and the shape [see Fig. 8(f)] is much closer to the real river [see Fig. 8(g)] after geometric calibration. Fig. 9(a) and (d) shows the locations of the two examined areas in Beijing and Xinjiang, and the road [see Fig. 9(b)] and reservoir [see Fig. 9(f)] cannot connect in the adjacent images before calibration. However, the shapes of the road [see Fig. 9(c)] and reservoir [see Fig. 9(g)], after geometric calibration, are more consistent with those in the reference multispectral image [see Fig. 9(d) and (h)], indicating that this improved model helps the calibrated images to recover geometric consistency.

IV. Discussion

This article constructed an improved geometric calibration model of SAR images, which does not need long-delayed meteorological data and geometric calibration fields. This model is suitable for the geometric calibration of large-scale SAR images (e.g., China's Gaofen-3 and Tianhui-2), and can also be applied to the geometric calibration of SAR satellites worldwide (e.g., TerraSAR-X). The geometric positioning accuracy of Gaofen-3 SAR images was verified in YRD between July 2018 and May 2019. The results show that the rms of the geometric positioning accuracy of Gaofen-3 is about 38.4 m before geometric calibration (cf., Table III), but it is reduced to smaller than 10 m after geometric calibration (see Fig. 5). One contribution of this article is that the proposed model, for the first time, uses SAM-S for the tropospheric delay correction in the SAR geometric calibration, and another is that the development of joint calibration scenarios with different SAR image combinations provides a more reliable geometric calibration for large-scale areas.

Because the atmosphere is highly complex, it is very difficult for current numerical weather products to provide high precision, high spatial resolution atmospheric parameters in near real-time [59], [60]. The SAM-S method can achieve well estimated atmospheric delay correction when the earth's atmosphere is calm. Although the global weather reanalysis products can achieve better estimation in case of greatly changing weather [37], [43], there is often a lag of several months in the release of these products. Thus, this cannot be readily used to perform timely estimation of geometric calibration parameters. The SAM-S method in this article only lead to very minor differences in the atmospheric delay estimation compared with the IGS products (see Table II), indicating the effectiveness of the SAM-S estimation. This article focused on the method development of the geometric calibration of large-scale SAR images by compromising the image positioning accuracy and the cost; this means that this model does not need the long-delayed meteorological data and geometric calibration fields. Also, obvious differences in positioning accuracy are found before and after considering the atmospheric delay corrections (the first-row versus the second-row in Fig. 10), indicating the reliability of the atmospheric delay correction method. In case of no atmospheric delay correction, the number of images included in the modeling does not make substantial differences to the geometric calibration (the first row in Fig. 10). When considering the atmospheric delay correction, more images included in the modeling can substantially reduce the positioning errors as shown by the standard deviation and the rms (the second row in Fig. 10). After considering atmospheric delay correction, the mean positioning accuracy decreased from ∼5.2 m to ∼6.3 m, but the rms of all combinations decreased from ∼6.5 m to ∼6.0 m. This indicates that, based on the SAM-S method, the geometric calibration resulted in a more robust estimation of SAR imaging system errors, thus improving the calibration performance for most of the SAR images.

In fact, one-by-one calibration is the best scenario, however, it requires a large number of GCPs and SAR images, which cannot be completed in actual data production, especially in

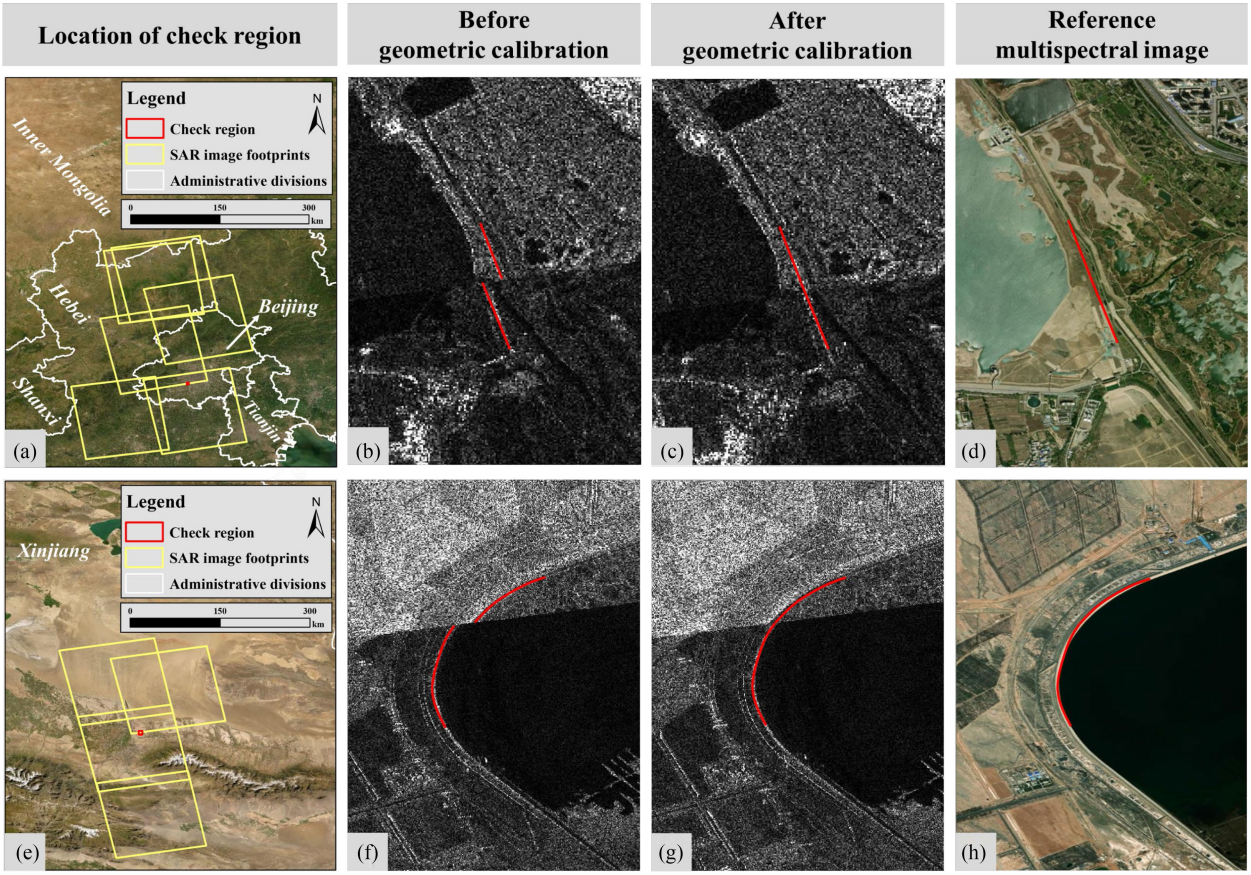

Fig. 9. Geometric consistency of adjacent images is improved after geometric calibration in Beijing and Xinjiang.

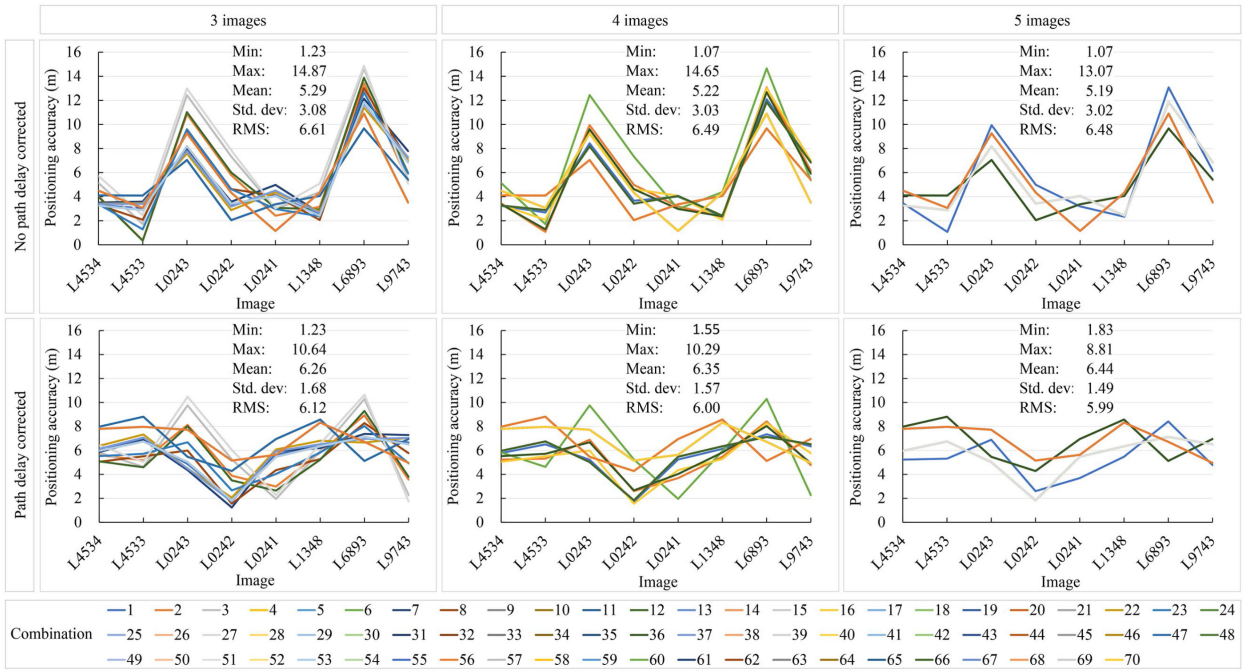

Fig. 10. Comparison of positioning accuracy before and after considering the atmospheric delay corrections as well as for each SAR image under different calibration scenarios.

TABLE V
MODEL PERFORMANCE ASSESSMENT OF IMAGES OF DIFFERENT IMAGING MODES

Image	The one-by-one calibration scenario				The joint calibration scenario			
	Slant range correction (m)	Imaging time correction (s)	Positioning accuracy (m)		Slant range correction (m)	Imaging time correction (s)	Positioning accuracy (m)	
			Before	After			Before	After
L9244 (QPSI)	-13.55	-0.0007	24.61	6.94	-13.55	-0.0007	19.48	4.32
L9245 (QPSI)	-17.16	-0.0006	28.41	5.62			19.34	4.74
L5285 (SS)	-15.02	-0.0052	26.21	6.51			21.23	3.59
L2205 (SS)	-13.17	-0.0061	26.38	6.58	-13.62	-0.0054	23.64	4.96
L2206 (SS)	-13.55	-0.0007	24.61	6.94			21.93	7.29
L2078 (FSII)	-17.81	-0.0059	17.97	5.91			17.97	4.71
L7076 (FSII)	-17.04	-0.0041	26.93	4.35	-16.91	-0.0039	26.93	4.21
L7078 (FSII)	-16.91	-0.0039	28.04	5.82			28.04	5.82
L4384 (FSII)	-18.98	-0.0050	26.95	5.49	-18.98	-0.0050	26.95	8.29
L4385 (FSII)	-16.40	-0.0040	25.83	7.27			25.83	7.27
RMS (QPSI)	/	/	19.41	4.72	/	/	19.41	4.53
RMS (SS)	/	/	22.07	5.14	/	/	22.50	5.32
RMS (FSII)	/	/	25.40	5.84	/	/	25.41	6.25

large-scale or global calibration. The rms of the positioning accuracy of one-by-one calibration is 5.47 m, while the rms of the joint calibration with all images is 11.41 m (cf., Table III). The decreases from 5.47 m to 11.41 m would likely be attributed to the bandwidth effects because the joint calibration for the images of 60 MHz is 6.90 m (rms), much better than the calibration using all images (cf., Table III). Further analysis shows that the positioning accuracy of the calibrated images for all combinations is about 6.0 ± 2.7 m with a 95% confidence interval. These indicate that the positioning accuracy ($\sim$6.90 m) after geometric calibration is much better than the nominal spatial resolution (10 m) of Gaofen-3 FSII images, indicating the model has satisfactory application ability.

The calibration accuracy is affected by the GCP selection, the atmospheric delay estimation and unknown errors. The results show that the rms of different image combinations is about 6 m (see Fig. 5), and the maximum error of all images is smaller than 11 m (see Fig. 10). The enlarged areas (cf., Fig. 7) show that the Gaofen-3 images can produce seamless scenes after geometric calibration, and two selected areas show that, after calibration, the geometric distortion is corrected and the shapes in the SAR images are close to the ground targets (see Fig. 8). Because GCPs were collected from aerial orthophotos with a positioning accuracy of about 1 m, the accuracy of these GCPs can be considered as twice (i.e., 2 m) the standard deviation of the aerial orthophotos. The elevation is collected from SRTM DEM, which has a spatial resolution of 90 m and an absolute height error of smaller than 16 m [61]. Geometric calibration accuracy is improved when higher elevation accuracy DEMs are applied [26].

Large facilities such as wind turbines and bridge piers can be selected as candidates for GCPs to ensure uniform distribution. Although the accuracy of these GCPs may be reduced due to phase center offset, background scattering, and image distortion and noise, this does not deny their potential to provide useful ground control information. The GWC method was applied to search for the strongest scattering point, and the accuracy of its phase center positioning can reach about 0.1 pixels. For large facilities, the phase center offset of the wind turbine and bridge pier causes an error of fewer than 0.5 pixels [cf., Fig. 4(a)–(b), (e)–(f)], the scattering from the surrounding objects causes an error of about 0.1 pixels, and the image distortion and noise causes an error of about 0.5 pixels. Therefore, the accuracy of GCPs in SAR images for these large facilities is about 0.7 to 1.1 pixels. For point targets [cf., Fig. 4(c)–(d), (g)–(h)], the phase center offset is small (about 0.2 pixels), the scattering from the surrounding objects causes an error of $\sim$0.1 pixels, and image distortion and noise cause an error of $\sim$0.5 pixels. Therefore, the accuracy of GCPs of these point targets in SAR images is about 0.9 pixels. All these suggest that the accuracy of GCPs in this article is about 1 pixel.

In addition, the residuals of atmospheric delay estimation may lead to positioning biases, where the tropospheric delay error may cause 1 m bias and the ionospheric delay error may cause additional bias. The ionospheric delay correction was conducted using a simple Klobuchar model, which can only capture 50% of ionospheric range error worldwide [62], [63]. The errors are also from unknown or random errors that cannot be well modeled to date [28], [64]. Although the abovementioned errors have not been well captured in this article, this improved method can provide better SAR images in a large region like YRD and should be useful elsewhere for the geometric calibration of SAR images.

Applicability is an important feature of geometric calibration models. In this article, geometric calibration was performed in two distant regions, Beijing and Xinjiang, to verify the applicability of the improved geometric calibration model (see Table IV). The results show that this geometric calibration model can effectively improve the positioning accuracy of SAR images. The applicability of the model to SAR images with different imaging modes was further evaluated (i.e., QPSI, SS, and FSII). After geometric calibration, the rmss of all images for all three

imaging modes were better than 6.3 m (see Table V). Due to errors in the selection of GCPs and checkpoints, as well as differences in imaging bandwidth, there are also differences in the positioning accuracy after calibration for the same imaging mode (e.g., L4384 and L4385). The improvement in image positioning accuracy for the three imaging modes demonstrates the good applicability of the improved geometric calibration model, while further evaluation is needed for higher resolution images (e.g., spotlight images).

V. Conclusion

SAR satellites have the advantages of earth observation regardless of the weather and solar radiation conditions, and the SAR images have already become powerful datasets for global mapping of ground targets. However, SAR imaging is commonly affected by many influencing factors such as the space environments with drastic temperature changes, thus, geometric calibration should be conducted before mapping and application. In this article, an improved geometric calibration model of SAR images was constructed, it does not need long-delayed meteorological data and geometric calibration fields. The method was then applied to China's Gaofen-3 satellite with a case study in YRD where the weather is cloudy and rainy.

Contributions of this article include that 1) the proposed geometric calibration model can be applied to geometric calibration tasks worldwide without the support of long-delayed meteorological data and geometric calibration fields, 2) the calibration scenarios can well verify the effectiveness of the geometric calibration model in large-scale areas, and 3) after geometric calibration, the positioning accuracy of Gaofen-3 images in YRD is much better than that before geometric calibration. Importantly, the atmospheric delay correction improves the stability of geometric calibration and the positioning accuracy of SAR images, and the geometric distortion in SAR images is significantly eliminated after geometric calibration. The positioning accuracy improvement of Gaofen-3 images can help improve their application potential in global remote sensing mapping, land-use change monitoring, and important ground target detection. The proposed geometric calibration method can also be applied to other SAR missions such as ERS, RADARSAT, and TerraSAR-X.

References

[1] F. Caltagirone, "Status, results and perspectives of the italian earth observation SAR COSMO - SkyMed," in *Proc. Eur. Radar Conf.*, 2009, pp. 330–334.

[2] M. Antoniou et al., "Passive SAR satellite constellation for near-persistent earth observation: Prospects and issues," *IEEE Aerosp. Electron. Syst. Mag.*, vol. 33, no. 12, pp. 4–15, Dec. 2018.

[3] S. Huber, F. Q. de Almeida, M. Villano, M. Younis, G. Krieger, and A. Moreira, "Tandem-L: A technical perspective on future spaceborne SAR sensors for earth observation," *IEEE Trans. Geosci. Remote Sens.*, vol. 56, no. 8, pp. 4792–4807, Aug. 2018.

[4] K. Tomiyasu, "Tutorial review of synthetic-aperture radar (SAR) with applications to imaging of the ocean surface," *Proc. IEEE*, vol. 66, no. 5, pp. 563–583, May 1978.

[5] X. Tang, T. Li, X. Gao, Q. Chen, and X. Zhang, "Research on key technologies of precise InSAR surveying and mapping applications using automatic SAR imaging," *J. Geodesy Geoinformation Sci.*, vol. 2, no. 2, pp. 27–37, 2019.

[6] F. Dell'Acqua, C. Bignami, M. Chini, G. Lisini, D. A. Polli, and S. Stramondo, "Earthquake damages rapid mapping by satellite remote sensing data: L'Aquila april 6th, 2009 event," *IEEE J. Sel. Topics Appl. Earth Observ. Remote Sens.*, vol. 4, no. 4, pp. 935–943, Dec. 2011.

[7] M. Huber et al., "Shaping the global high-resolution TanDEM-X digital elevation model," *IEEE J. Sel. Topics Appl. Earth Observ. Remote Sens.*, vol. 14, pp. 7198–7212, Jul. 2021, doi: 10.1109/JSTARS.2021.3095178.

[8] C. Villamil Lopez and U. Stilla, "Monitoring of oil tank filling with spaceborne SAR using coherent scatterers," *IEEE J. Sel. Topics Appl. Earth Observ. Remote Sens.*, vol. 14, pp. 5638–5655, May 2021, doi: 10.1109/JSTARS.2021.3082181.

[9] M. Deng, G. Zhang, R. Zhao, S. Li, and J. Li, "Improvement of gaofen-3 absolute positioning accuracy based on cross-calibration," *Sensors*, vol. 17, no. 12, pp. 2903–2917, 2017.

[10] C. Ding, J. Liu, B. Lei, and X. Qiu, "Preliminary exploration of systematic geolocation accuracy of GF-3 SAR satellite system," *J. Radars*, vol. 6, no. 1, pp. 11–16, 2017.

[11] J. Hueso Gonzalez, M. Bachmann, G. Krieger, and H. Fiedler, "Development of the TanDEM-X calibration concept: Analysis of systematic errors," *IEEE Trans. Geosci. Remote Sens.*, vol. 48, no. 2, pp. 716–726, Feb. 2010.

[12] X. Zhou, Q. Zeng, J. Jiao, Q. Wang, S. Xiong, and S. Gao, "Field calibration and validation of Radarsat-2," in *Proc. IEEE Int. Geosci. Remote Sens. Symp.*, 2013, pp. 4451–4454.

[13] M. Schwerdt, B. Brautigam, M. Bachmann, B. Doring, D. Schrank, and J. Hueso Gonzalez, "Final TerraSAR-X calibration results based on novel efficient methods," *IEEE Trans. Geosci. Remote Sens.*, vol. 48, no. 2, pp. 677–689, Feb. 2010.

[14] G. Zhang et al., "Stability analysis of geometric positioning accuracy of YG-13 satellite," *IEEE Trans. Geosci. Remote Sens.*, vol. 60, 2022, Art. no. 5200112, doi: 10.1109/TGRS.2020.3042649.

[15] B. Brautigam, M. Schwerdt, M. Bachmann, and B. Doring, "Results from geometric and radiometric calibration of TerraSAR-X," in *Proc. Eur. Radar Conf.*, 2007, pp. 87–90.

[16] R. Zandbergen, J. M. Dow, M. Romay Merino, R. Píriz, and F. Martínez Fadrique, "ERS-1 and ERS-2 tandem mission: Orbit determination, prediction and maintenance," *Adv. Space Res.*, vol. 19, no. 11, pp. 1649–1653, 1997.

[17] J. J. Mohr and S. N. Madsen, "Geometric calibration of ERS satellite SAR images," *IEEE Trans. Geosci. Remote Sens.*, vol. 39, no. 4, pp. 842–850, Apr. 2001.

[18] M. Shimada, O. Isoguchi, T. Tadono, and K. Isono, "PALSAR radiometric and geometric calibration," *IEEE Trans. Geosci. Remote Sens.*, vol. 47, no. 12, pp. 3915–3932, Dec. 2009.

[19] T. Toutin, R. Chénier, C. Schmitt, and I. Zakharov, "Calibration of radargrammetric DEMs from RADARSAT-2 high-resolution and fine-quad modes," in *Proc. IEEE Int. Geosci. Remote Sens. Symp.*, 2009, pp. V-41–V-43.

[20] A. Schubert, D. Small, M. Jehle, and E. Meier, "COSMO-skymed, TerraSAR-X, and RADARSAT-2 geolocation accuracy after compensation for earth-system effects," in *Proc. IEEE Int. Geosci. Remote Sens. Symp.*, 2012, pp. 3301–3304.

[21] A. Schubert, N. Miranda, D. Geudtner, and D. Small, "Sentinel-1A/B combined product geolocation accuracy," *Remote Sens.*, vol. 9, no. 6, pp. 607–622, 2017.

[22] A. Schubert, D. Small, N. Miranda, D. Geudtner, and E. Meier, "Sentinel-1A product geolocation accuracy: Commissioning phase results," *Remote Sens.*, vol. 7, no. 7, pp. 9431–9449, 2015.

[23] M. Eineder, C. Minet, P. Steigenberger, X. Cong, and T. Fritz, "Imaging geodesy—Toward centimeter-level ranging accuracy with TerraSAR-X," *IEEE Trans. Geosci. Remote Sens.*, vol. 49, no. 2, pp. 661–671, Feb. 2011.

[24] X. Zhou, Q. Zeng, J. Jiao, Q. Wang, S. Xiong, and S. Gao, "Research on Space-borne SAR field calibration Experiment—A case study of TerraSAR-X field calibration," *Remote Sens. Technol. Appl.*, vol. 29, no. 5, pp. 711–718, 2014.

[25] J. Sun, W. Yu, and Y. Deng, "The SAR payload design and performance for the GF-3 mission," *Sensors*, vol. 17, no. 10, 2017, Art. no. 2419.

[26] G. Lv, X. Tang, B. Ai, T. Li, and Q. Chen, "Hybrid geometric calibration method for multi-platform spaceborne SAR image with sparse GCPs," *Int. Arch. Photogrammetry Remote Sens. Spatial Inf. Sci.*, vol. XLII-3, pp. 1221–1228, 2018.

[27] L. Ding, Q. Tao, T. Li, Q. Chen, and Y. Cen, "A joint geometric calibration technique for GF-3 SAR image in wide area," *Acta Geodaetica et Cartographica Sinica*, vol. 49, no. 5, pp. 598–610, 2020.

[28] R. Zhao, G. Zhang, M. Deng, K. Xu, and F. Guo, "Geometric calibration and accuracy verification of the GF-3 satellite," *Sensors*, vol. 17, no. 9, pp. 1977–1989, 2017.
[29] M. C. Garthwaite, M. Thankappan, M. L. Williams, S. Nancarrow, A. Hislop, and J. Dawson, "Corner reflectors for the australian geophysical observing system and support for calibration of satellite-borne synthetic aperture radars," in *Proc. IEEE Int. Geosci. Remote Sens. Symp.*, 2013, pp. 266–269.
[30] G. Zhang et al., "Block adjustment without GCPs for chinese spaceborne SAR GF-3 imagery," *Sensors*, vol. 18, no. 11, pp. 4023–4037, 2018.
[31] T. Wang, G. Zhang, L. Yu, R. Zhao, M. Deng, and K. Xu, "Multi-Mode GF-3 satellite image geometric accuracy verification using the RPC model," *Sensors*, vol. 17, no. 9, 2017, Art. no. 2005.
[32] M. Jehle, D. Perler, D. Small, A. Schubert, and E. Meier, "Estimation of atmospheric path delays in TerraSAR-X data using models vs. Measurements," *Sensors*, vol. 8, no. 12, pp. 8479–8491, 2008.
[33] A. Schubert, M. Jehle, D. Small, and E. Meier, "Influence of atmospheric path delay on the absolute geolocation accuracy of TerraSAR-X high-resolution products," *IEEE Trans. Geosci. Remote Sens.*, vol. 48, no. 2, pp. 751–758, Feb. 2010.
[34] R. Zhao, G. Zhang, M. Deng, F. Yang, Z. Chen, and Y. Zheng, "Multimode hybrid geometric calibration of spaceborne SAR considering atmospheric propagation delay," *Remote Sens.*, vol. 9, no. 5, pp. 464–482, 2017.
[35] R. Jolivet, R. Grandin, C. Lasserre, M.-P. Doin, and G. Peltzer, "Systematic InSAR tropospheric phase delay corrections from global meteorological reanalysis data," *Geophysical Res. Lett.*, vol. 38, no. 17, pp. 1–6, 2011.
[36] J. Foster, J. Kealy, T. Cherubini, S. Businger, Z. Lu, and M. Murphy, "The utility of atmospheric analyses for the mitigation of artifacts in InSAR," *J. Geophysical Res., Solid Earth*, vol. 118, no. 2, pp. 748–758, 2013.
[37] C. Yu, Z. Li, N. T. Penna, and P. Crippa, "Generic atmospheric correction model for interferometric synthetic aperture radar observations," *J. Geophysical Res., Solid Earth*, vol. 123, no. 10, pp. 9202–9222, 2018.
[38] D. P. Dee et al., "The ERA-Interim reanalysis: Configuration and performance of the data assimilation system," *Quart. J. Roy. Meteorological Soc.*, vol. 137, no. 656, pp. 553–597, 2011.
[39] D. Jiao, N. Xu, F. Yang, and K. Xu, "Evaluation of spatial-temporal variation performance of ERA5 precipitation data in China," *Sci. Rep.*, vol. 11, no. 1, pp. 17956–17969, 2021.
[40] W. Wang, J. Liu, and X. Qiu, "Decimeter-Level geolocation accuracy updated by a parametric tropospheric model with GF-3," *Sensors*, vol. 18, no. 7, 2018, Art. no. 2197.
[41] J. Liu, X. Chen, J. Sun, and Q. Liu, "An analysis of GPT2/GPT2w+Saastamoinen models for estimating zenith tropospheric delay over asian area," *Adv. Space Res.*, vol. 59, no. 3, pp. 824–832, 2017.
[42] U. Beisla and U. Tempelmanna, "Estimation of the atmospheric refraction effect in airborne images using radiosonde data," *ISPRS - Int. Arch. Photogrammetry, Remote Sens. Spatial Inf. Sci.*, vol. XLI-B1, pp. 281–286, 2016.
[43] B. Chen and Z. Liu, "A comprehensive evaluation and analysis of the performance of multiple tropospheric models in China region," *IEEE Trans. Geosci. Remote Sens.*, vol. 54, no. 2, pp. 663–678, Feb. 2016.
[44] J. Zhang, H. Gu, W. Hou, and C. Cheng, "Technical progress of China's national remote sensing mapping: From mapping western China to national dynamic mapping," *Geo-Spatial Inf. Sci.*, vol. 24, no. 1, pp. 121–133, 2021.
[45] M. Xu, Z. Xia, F. Zhang, K. Li, and C. Xie, "Multi-Temporal polarimetric SAR and optical data fusion for land cover mapping in southwest China," in *Proc. Int. Conf. Multimedia Technol.*, 2010, pp. 1–4.
[46] A. Moreira, P. Prats-Iraola, M. Younis, G. Krieger, I. Hajnsek, and K. P. Papathanassiou, "A tutorial on synthetic aperture radar," *IEEE Geosci. Remote Sens. Mag.*, vol. 1, no. 1, pp. 6–43, Mar. 2013.
[47] M. Zhang, F. Chen, B. Tian, and D. Liang, "Multi-temporal SAR image classification of coastal plain wetlands using a new feature selection method and random forests," *Remote Sens. Lett.*, vol. 10, no. 3, pp. 312–321, 2019.
[48] M. I. Skolnik, *Radar Handbook*, 2nd ed. New York, NY, USA: McGraw-Hill, 1990.
[49] M. Bevis et al., "GPS meteorology: Mapping zenith wet delays onto precipitable water," *J. Appl. Meteorol. Climatol.*, vol. 33, no. 3, pp. 379–386, 1994.
[50] M. J. Fernandes, C. Lázaro, and T. Vieira, "On the role of the troposphere in satellite altimetry," *Remote Sens. Environ.*, vol. 252, 2021, Art. no. 112149, doi: 10.1016/j.rse.2020.112149.
[51] H. Breit, T. Fritz, U. Balss, M. Lachaise, A. Niedermeier, and M. Vonavka, "TerraSAR-X SAR processing and products," *IEEE Trans. Geosci. Remote Sens.*, vol. 48, no. 2, pp. 727–740, Feb. 2010.
[52] J. Liu, X. Qiu, B. Han, and D. Xiao, "Study on geo-location of sliding spotlight mode of GF-3 satellite," in *Proc. IEEE 5th Asia-Pacific Conf. Synthetic Aperture Radar*, 2015, pp. 417–420.
[53] J. C. Curlander, "Location of spaceborne sar imagery," *IEEE Trans. Geosci. Remote Sens.*, vol. GE-20, no. 3, pp. 359–364, Jul. 1982.
[54] L. Zhang, T. Balz, and M. Liao, "Satellite SAR geocoding with refined RPC model," *ISPRS J. Photogrammetry Remote Sens.*, vol. 69, pp. 37–49, 2012.
[55] M. Shimada, "Radiometric and geometric calibration of JERS-1 SAR," *Adv. Space Res.*, vol. 17, no. 1, pp. 79–88, 1996.
[56] W. M. Moon, G. Staples, D. Kim, S. Park, and K. Park, "RADARSAT-2 and coastal applications: Surface wind, waterline, and intertidal flat roughness," *Proc. IEEE*, vol. 98, no. 5, pp. 800–815, May 2010.
[57] F. Yang, J. Guo, J. Li, C. Zhang, and M. Chen, "Assessment of the troposphere products derived from VMF data server with ERA5 and IGS data over China," *Earth Space Sci.*, vol. 8, no. 8, 2021, Art. no. e2021EA001815.
[58] G. Johnston, A. Riddell, and G. Hausler, "The international GNSS service," in *Springer Handbook of Global Navigation Satellite Systems*, P. J. G. Teunissen and O. Montenbruck, Eds. Cham, Switzerland: Springer, 2017, pp. 967–982.
[59] P. Bauer, A. Thorpe, and G. Brunet, "The quiet revolution of numerical weather prediction," *Nature*, vol. 525, no. 7567, pp. 47–55, 2015.
[60] T. N. Palmer, "Stochastic weather and climate models," *Nature Rev. Phys.*, vol. 1, no. 7, pp. 463–471, 2019.
[61] T. G. Farr et al., "The shuttle radar topography mission," *Rev. Geophys.*, vol. 45, no. 2, pp. 1–33, 2007, doi: 10.1029/2005RG000183.
[62] N. Wang, Y. Yuan, Z. Li, and X. Huo, "Improvement of klobuchar model for GNSS single-frequency ionospheric delay corrections," *Adv. Space Res.*, vol. 57, no. 7, pp. 1555–1569, 2016.
[63] B. Bidaine, M. Lonchay, and R. Warnant, "Galileo single frequency ionospheric correction: Performances in terms of position," *GPS Solutions*, vol. 17, no. 1, pp. 63–73, 2013.
[64] G. Zhang, M. Deng, C. Cai, and R. Zhao, "Geometric self-calibration of yaogan-13 images using multiple overlapping images," *Sensors*, vol. 19, no. 10, pp. 2367–2377, 2019.

Yongjiu Feng received the Ph.D. degree in geomatics from Tongji University, Shanghai, China, in 2009.

He is currently a Professor and Associate Dean with the College of Surveying and Geo-Informatics, Tongji University. His research interests include spatial modeling, synthetic aperture radar, and radar detection of the moon and deep space.

Zhenkun Lei received the M.S. degree in marine sciences from Shanghai Ocean University, Shanghai, China, in 2021. He is currently working toward the Ph.D. degree in surveying and mapping science and technology with Tongji University, Shanghai, China.

Xiaohua Tong (Senior Member, IEEE) received the Ph.D. degree in geomatics from Tongji University, Shanghai, China, in 1999.

He is currently a Professor with the College of Surveying and Geo-Informatics, Tongji University. His research interests include photogrammetry and remote sensing, trust in spatial data, and image processing for high-resolution satellite images.

Mengrong Xi is currently working toward the Ph.D. degree in geomatics engineering with Tongji University, Shanghai, China.

Pengshuo Li received the B.E. degree in geomatics engineering from Tongji University, Shanghai, China, in 2021. He is currently working toward the M.S. degree in surveying and mapping science and technology with Tongji University, Shanghai, China.